

Research Article

A General 3D Nonstationary Vehicle-to-Vehicle Channel Model Allowing 3D Arbitrary Trajectory and 3D-Shaped Antenna Array

Qiuming Zhu ¹, Weidong Li ¹, Ying Yang¹, Dazhuan Xu ¹, Weizhi Zhong ²,
and Xiaomin Chen ¹

¹Key Laboratory of Dynamic Cognitive System of Electromagnetic Spectrum Space,

College of Electronic and Information Engineering, Nanjing University of Aeronautics and Astronautics, Nanjing 211106, China

²Key Laboratory of Dynamic Cognitive System of Electromagnetic Spectrum Space, College of Astronautics,
Nanjing University of Aeronautics and Astronautics, Nanjing 211106, China

Correspondence should be addressed to Qiuming Zhu; zhuqiuming@nuaa.edu.cn

Received 1 May 2019; Accepted 25 August 2019; Published 20 October 2019

Guest Editor: Danping He

Copyright © 2019 Qiuming Zhu et al. This is an open access article distributed under the Creative Commons Attribution License, which permits unrestricted use, distribution, and reproduction in any medium, provided the original work is properly cited.

Most of the existing channel model for multiple-input multiple-output (MIMO) vehicle-to-vehicle (V2V) communications only considered that the terminals were equipped with linear antenna arrays and moved with fixed velocities. Nevertheless, under the realistic environment, those models are not practical since the velocities and trajectories of mobile transmitter (MT) and mobile receiver (MR) could be time-variant and unpredictable due to the complex traffic conditions. This paper develops a general 3D nonstationary V2V channel model, which is based on the traditional geometry-based stochastic models (GBSMs) and the twin-cluster approach. In contrast to the traditional models, this new model is characterized by 3D scattering environments, 3D antenna arrays, and 3D arbitrary trajectories of both terminals and scatterers. The calculating methods of channel parameters are also provided. In addition, the statistical properties, i.e., spatial-temporal correlation function (STCF) and Doppler power spectrum density (DPSD), are derived in detail. Simulation results have demonstrated that the output statistical properties of the proposed model agree well with the theoretical and measured results, which verifies the effectiveness of theoretical derivations and channel model as well.

1. Introduction

Vehicle-to-vehicle (V2V) communications can improve the safety of life and property by collecting and exchanging environment information under complex traffic [1]. Meanwhile, multiple-input multiple-output (MIMO) technologies can expand the capacity and improve the communication efficiency. It is promising to apply MIMO technologies to V2V communications. To provide reasonable references for developing, analyzing, and testing V2V communication systems, a general, accurate, and easy-to-use channel model is required. Moreover, the movements, insufficient antenna space, and lack of rich scattering should be considered in channel modeling and statistical property analysis [2–7].

The wide-sense stationary (WSS) assumption was adopted in the traditional geometry-based stochastic models (GBSMs) [5, 8]. Nevertheless, the authors in [9, 10] found that the WSS was only suitable for short distances between transmitters and receivers based on the measured data. Several GBSMs for nonstationary V2V channels are proposed in the literature [11–25]. Among them, 2D nonstationary V2V GBSMs with fixed clusters [11, 12] or moving scatterers [13] were studied and the statistical properties, i.e., the temporal correlation function (TCF), spatial correlation function (SCF), and Doppler power spectrum density (DPSD), were also analyzed. The authors in [14] proposed a 2D V2V channel model with random movement scatterers. The aforementioned 2D channel models were only considered on the horizontal plane. Under

the realistic scenarios, the scatterers, e.g., vehicles, pedestrian, and infrastructures, may distribute or move in the 3D space. Meanwhile, the authors in [7] have proved that the 3D channel model is more accurate than the 2D ones for evaluating the system performance. By extending the scatterers distributed on the surface of 3D regular shapes, i.e., a hemisphere [15], two cylinders [16, 17], two spheres [18], an elliptic-cylinder [19], a rectangular tunnel [20], several 3D nonstationary V2V channel models were proposed recently. In [21], the authors proposed a 3D irregular-shaped GBSM for nonstationary V2V channels. Some 3D cluster-based nonstationary V2V channel models can also be addressed in [22–25]. However, the output phases related to the Doppler frequencies in [11–25] were inaccurate compared with the theoretical results [26, 27]. The authors in [28, 29] modified the phase item to overcome this shortcoming, but it is only suitable for 2D scattering environments. A modified 3D channel model with accurate Doppler frequency can be addressed in [30].

Note that most of the existing V2V channel models [11–26] only took the fixed velocities of the mobile transmitter (MT) and mobile receiver (MR) into account. However, under realistic traffic environments, the velocities of MT and MR could be time-variant. Although the time-variant velocities were considered in [29, 31–33], their trajectories were 2D. Meanwhile, the models in the literature [11–33] only considered 2D or even 1D antenna arrays for simplicity. With the development of antenna technologies, 3D-shaped antenna arrays begin to be used in MIMO communication systems. Very recently, a general 3D nonstationary GBSM between base station and MT with 3D arbitrary trajectories and 3D antenna arrays was proposed in [34]. This idea was adopted by [35] to model the 3D V2V channels allowing MT and MR with 3D arbitrary trajectories. However, the details of channel parameter computation and theoretical analyses of SCF, TCF, and DPSD were lacked. This paper aims at filling these gaps. The major contributions and novelties are summarized as follows:

- (1) Combining the GBSM and twin-cluster approach [36], a general 3D V2V channel model was proposed. The 3D antenna array and 3D arbitrary trajectory of each terminal are allowed under the 3D scattering environment, which guarantees the proposed model is more general and has the nonstationary aspect.
- (2) The upgraded computation procedure of channel parameters for the proposed model, such as the number of paths, path delays, and path powers, are developed and analyzed in detail.
- (3) The theoretical closed-form expressions of statistical properties, i.e., the SCFs, TCFs, and DPSDs are investigated and verified by the simulation method and measurement data.

This paper is structured as follows. Section 2 presents a 3D general V2V channel model characterized by nonstationary aspect and generalization. The channel parameter updating algorithms are given in Section 3. In Section 4, the theoretical SCFs, TCFs, and DPSDs of the

proposed model are derived in detail. Section 5 shows and compares the simulated results with the derived ones and measured data. Finally, the conclusions are drawn in Section 6.

2. 3D Nonstationary GBSM for V2V Channels

Figure 1 shows a typical 3D V2V communication system between the MT and MR, which is characterized by 3D arbitrary trajectories and 3D antenna arrays. The MT and MR are configured with S and U antennas, respectively. In the figure, the coordinate systems at the MT and MR with the centers of corresponding terminals are named as xyz and $\tilde{x}\tilde{y}\tilde{z}$, respectively. Suppose that the travel directions of the MT and MR at the initial time correspond to x -axis's direction, respectively. Due to the movement and rotation of two coordinate systems, the antenna element of MT or MR is 3D and time-variant and can be expressed by $\mathbf{d}_s^{\text{MT}}(t) = [d_{s,x}^{\text{MT}}(t), d_{s,y}^{\text{MT}}(t), d_{s,z}^{\text{MT}}(t)]^T$ or $\mathbf{d}_u^{\text{MR}}(t) = [d_{u,x}^{\text{MR}}(t), d_{u,y}^{\text{MR}}(t), d_{u,z}^{\text{MR}}(t)]^T$. Figure 1 shows that between the MT and MR, there are many propagation paths and subpaths (or rays). The 3D location of the first cluster S_n^{MT} or the last cluster S_n^{MR} affects the corresponding elevation angles, such as elevation angle of departure (EAoD) $\theta_{n,m}^{\text{MT}}(t)$ and elevation angle of arrival (EAoA) $\theta_{n,m}^{\text{MR}}(t)$, and azimuth angles, such as the azimuth angle of departure (AAoD) $\phi_{n,m}^{\text{MT}}(t)$ and the azimuth angle of arrival (AAoA) $\phi_{n,m}^{\text{MR}}(t)$. In addition, by adopting twin-cluster approach, the rest clusters can be viewed as a virtual link [36]. In the figure, $\mathbf{v}^i(t)$ and $S_n^i(t)$, $i \in \{\text{MT}, \text{MR}\}$, represent time-variant velocities of i and S_n^i , respectively. Table 1 shows the detailed definitions of channel parameters.

Under the V2V communication scenario of Figure 1, the V2V MIMO channel can be modeled as [30]

$$\mathbf{H}\mathbf{t}, \tau = \begin{bmatrix} h_{1,1t,\tau} & h_{1,2t,\tau} & \cdots & h_{1,St,\tau} \\ h_{2,1t,\tau} & h_{u,St,\tau} & \cdots & h_{2,St,\tau} \\ \vdots & \vdots & \ddots & \vdots \\ h_{U,1t,\tau} & h_{U,2t,\tau} & \cdots & h_{U,St,\tau} \end{bmatrix}, \quad (1)$$

where $h_{u,s}(t, \tau)$ denotes the complex channel impulse response (CIR) between the transmitting antenna s ($s = 1, 2, \dots, S$) and receiving antenna u ($u = 1, 2, \dots, U$). In this paper, we modify the model of $h_{u,s}(t, \tau)$ in [30] and express it as

$$h_{u,s}(t, \tau) \triangleq \Pi_{T_0}(t) \sum_{n=1}^{N(t)} \sqrt{P_n(t)} \tilde{h}_{u,s,n}(t) \delta(\tau - \tau_n(t)), \quad (2)$$

where $\Pi_{T_0}(t)$ is a rectangular window function:

$$\Pi_{T_0}(t) \triangleq \begin{cases} 1, & 0 \leq t \leq T_0, \\ 0, & \text{otherwise,} \end{cases} \quad (3)$$

and it is introduced to limit the length of CIR, and thus, the large-scale variations can be negligible within the time interval; $N(t)$ represents the valid path number and is related to the path delay $\tau_n(t)$, path power $P_n(t)$, and normalized coefficient $\tilde{h}_{u,s,n}(t)$, which is expressed as

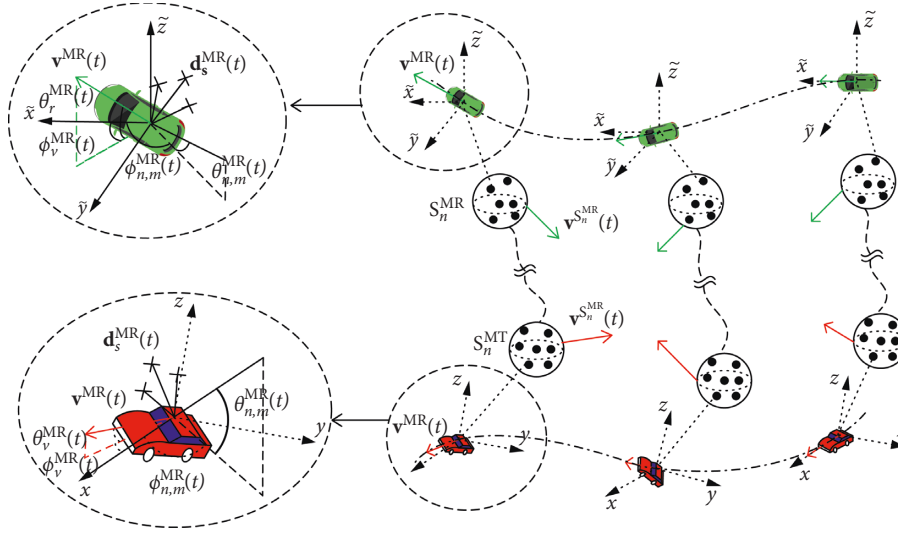


FIGURE 1: Typical 3D V2V communication system.

TABLE 1: Definitions of channel parameters.

$N(t)$	Valid path number
$P_n(t), \tau_n(t)$	The n th path power and delay
M	The number of subpaths
$\mathbf{d}_s^{\text{MT}}(t), \mathbf{d}_u^{\text{MR}}(t)$	Location vectors of transmitter antenna element s and receiver antenna element u , respectively
$\mathbf{L}^i(t), \mathbf{L}^{S_n^i}(t)$	Location vectors of i and S_n^i , $i \in \{\text{MT}, \text{MR}\}$, respectively
$\mathbf{v}^i(t), \mathbf{v}^{S_n^i}(t)$	Velocity vectors of i and S_n^i , $i \in \{\text{MT}, \text{MR}\}$, respectively
$\ \mathbf{v}^i(t)\ , \ \mathbf{v}^{S_n^i}(t)\ $	Speeds of i and S_n^i , $i \in \{\text{MT}, \text{MR}\}$, respectively
$\phi_v^i(t), \phi_v^{S_n^i}(t)$	Traveling azimuth angles of i and S_n^i , $i \in \{\text{MT}, \text{MR}\}$, respectively
$\theta_v^i(t), \theta_v^{S_n^i}(t)$	Traveling elevation angles of i and S_n^i , $i \in \{\text{MT}, \text{MR}\}$, respectively
$\tilde{\mathbf{s}}_{n,m}^i(t)$	Spherical unit vector of i along ray m of cluster n , $i \in \{\text{MT}, \text{MR}\}$
$\phi_{n,m}^{\text{MT}}(t), \theta_{n,m}^{\text{MT}}(t)$	Azimuth and elevation departure angles along ray m of cluster n , respectively
$\phi_{n,m}^{\text{MR}}(t), \theta_{n,m}^{\text{MR}}(t)$	Azimuth and elevation arrival angles along ray m of cluster n , respectively

$$\tilde{h}_{u,s,n}(t) = \lim_{M \rightarrow \infty} \sqrt{\frac{1}{M}} \sum_{m=1}^M e^{j(\Phi_{n,m}^{\text{D}}(t) + \Phi_{u,s,n,m}^{\text{L}}(t) + \Phi_{n,m}^{\text{I}})}, \quad (4)$$

where M denotes the subpath number, $\Phi_{n,m}^{\text{I}}$ stands for the random initial phase distributing over $[0, 2\pi)$ uniformly, and $\Phi_{n,m}^{\text{D}}(t)$ means the phase somehow affected by variant Doppler frequency. Here, we model $\Phi_{n,m}^{\text{D}}(t)$ as

$$\Phi_{n,m}^{\text{D}}(t) = k \int_0^t \mathbf{v}^{\text{MT}, S_n^{\text{MT}}}(t') \cdot \tilde{\mathbf{s}}_{n,m}^{\text{MT}}(t') + \mathbf{v}^{\text{SMR}, \text{MR}}(t') \cdot \tilde{\mathbf{s}}_{n,m}^{\text{MR}}(t') dt', \quad (5)$$

where $k = 2\pi f_c/c$ denotes the wave number with f_c and c representing the carrier frequency and light speed, respectively. $\mathbf{v}^{i, S_n^i}(t)$, $i \in \{\text{MT}, \text{MR}\}$, denotes the relative velocity between i and S_n^i . The departure or arrival angle unit

vector of the m th subpath within the n th path $\tilde{\mathbf{s}}_{n,m}^i(t)$ is defined as

$$\tilde{\mathbf{s}}_{n,m}^i(t) = \begin{bmatrix} \cos \theta_{n,m}^i(t) \cos \phi_{n,m}^i(t) \\ \cos \theta_{n,m}^i(t) \sin \phi_{n,m}^i(t) \\ \sin \theta_{n,m}^i(t) \end{bmatrix}. \quad (6)$$

In (4), $\Phi_{u,s,n,m}^{\text{L}}(t)$ denotes the offset phase caused by the movements of terminals:

$$\Phi_{u,s,n,m}^{\text{L}}(t) = k \cdot (\tilde{\mathbf{s}}_{n,m}^{\text{MT}}(t))^{\text{T}} \cdot \mathbf{R}_v^{\text{MT}}(t) \cdot \mathbf{d}_s^{\text{MT}, t_0} + k \cdot (\tilde{\mathbf{s}}_{n,m}^{\text{MR}}(t))^{\text{T}} \cdot \mathbf{R}_v^{\text{MR}}(t) \cdot \mathbf{d}_u^{\text{MR}, t_0}, \quad (7)$$

where $[\cdot]^{\text{T}}$ means transpose operation and $\mathbf{d}_s^{\text{MT}, t_0}$ represents sth antenna position at initial time instant. Similarly, $\mathbf{d}_u^{\text{MR}, t_0}$

represents the corresponding antenna position at initial corresponding time. Note that $\mathbf{R}_v^i(t)$ is a rotation matrix due to the 3D arbitrary trajectory, and it can be written as

$$\mathbf{R}_v^i(t) = \begin{bmatrix} \cos \theta_v^i(t) \cos \phi_v^i(t) - \sin \theta_v^i(t) \sin \phi_v^i(t) & -\sin \theta_v^i(t) \cos \phi_v^i(t) \\ \cos \theta_v^i(t) \sin \phi_v^i(t) \cos \phi_v^i(t) - \sin \theta_v^i(t) \sin \phi_v^i(t) & -\sin \theta_v^i(t) \sin \phi_v^i(t) \\ \sin \theta_v^i(t) & 0 & \cos \theta_v^i(t) \end{bmatrix}. \quad (8)$$

3. Time-Variant Channel Parameters

3.1. Path Number. The valid path number has been proved to be time-variant under V2V scenarios by the measured data in [37], due to the moving clusters and two terminals. In other words, the old disappearing clusters and new appearing ones are random. We model these with a Markov process [38]. λ_G is used to denote the birth rate, and λ_R denotes the death rate. The probability of each path remaining from t to $t + \Delta t$ is calculated as [19]

$$P_r(t; \Delta t) = e^{-\lambda_R P_c (\|\mathbf{v}^{\text{SMT}}(t)\| + \|\mathbf{v}^{\text{SMR}}(t)\|) \Delta t} \cdot e^{(-\lambda_R \|\mathbf{v}^{\text{MR}}(t) - \mathbf{v}^{\text{MT}}(t)\|) \Delta t}, \quad (9)$$

where P_c means the moving percentage and $\|\mathbf{v}^{\text{S}^i}(t)\|$, $i \in \{\text{MT}, \text{MR}\}$, represents clusters average speed. $N_{\text{new}}(t)$ is introduced to describe newly generated path number and calculated as

$$E\{N_{\text{new}}(t)\} = \frac{\lambda_G}{\lambda_R} (1 - P_r(t; \Delta t)). \quad (10)$$

Combining (9) with (10), the averaged path number can be expressed as

$$E\{N(t)\} = N(t - \Delta t) P_r(t; \Delta t) + E\{N_{\text{new}}(t)\} = \frac{\lambda_G}{\lambda_R}. \quad (11)$$

3.2. Delays and Powers. For the n th valid path, the total delay at time instant t consists of the first and last bounce delays and virtual link delay, and it is a function of total distance as

$$\tau_n(t) = \frac{\|\mathbf{L}^{\text{MT}}(t) - \mathbf{L}_n^{\text{SMT}}(t)\| + \|\mathbf{L}^{\text{MR}}(t) - \mathbf{L}_n^{\text{SMR}}(t)\|}{c} + \tilde{\tau}_n(t), \quad (12)$$

where $\mathbf{L}^i(t)$ and $\mathbf{L}_n^{\text{S}^i}(t)$, $i \in \{\text{MT}, \text{MR}\}$, mean the instantaneous locations of i and S_n^i and can be updated from the values of previous time instant by

$$\begin{aligned} \mathbf{L}^i(t) &= \mathbf{L}^i(t - \Delta t) + \mathbf{v}^i(t - \Delta t) \Delta t, \\ \mathbf{L}_n^{\text{S}^i}(t) &= \mathbf{L}_n^{\text{S}^i}(t - \Delta t) + \mathbf{v}^{\text{S}^i}(t - \Delta t) \Delta t, \end{aligned} \quad (13)$$

where $\tilde{\tau}_n(t)$ denotes the equivalent delay of virtual link and it can be updated by the first-order filtering method in [26] as follows:

$$\tilde{\tau}_n(t) = \tilde{\tau}_n(t - \Delta t) e^{-(\Delta t / \tau_{\text{dec}})} + \left(1 - e^{-(\Delta t / \tau_{\text{dec}})}\right) X, \quad (14)$$

where $X \sim U[\|\mathbf{L}^{\text{MT}}(t) - \mathbf{L}^{\text{MR}}(t)\|/c, \tau_{\text{max}}]$, in which τ_{max} denotes the maximum delay, and τ_{dec} denotes the decorrelation speed of time-variant delays. Based on the measurement-based method, we can get the averaged power as

$$P_n'(t) = e^{-\tau_n(t) (1 - r_{\text{DS}} / r_{\text{DS}} \sigma_{\text{DS}})} \times 10^{-\xi_n / 10}, \quad (15)$$

where ξ_n , r_{DS} , and σ_{DS} mean the shadowing degree, delay factor, and delay spread, respectively, which are all related with the environments. Finally, all the normalized power can be denoted as

$$P_n(t) = \frac{P_n'(t)}{\sum_{n=1}^N P_n'(t)}. \quad (16)$$

3.3. Time-Variant Angles. Measurements in [39] revealed that the azimuth and elevation angles at two terminals are not independent and cannot be depicted by two independent distributions such as Gaussian or Laplacian. In this paper, we take the 3D von Mises-Fisher (VMF) distribution to describe these two joint angles [40]. The probability density function (PDF) of VMF distribution can be expressed as [39]

$$p(\phi, \theta) = \frac{\kappa \cos \theta e^{\kappa (\cos \theta \cos \bar{\theta} \cos(\phi - \bar{\phi}) + \sin \theta \sin \bar{\theta})}}{4\pi \sinh(\kappa)}, \quad (17)$$

$$-\pi \leq \phi \leq \pi, \quad -\frac{\pi}{2} \leq \theta \leq \frac{\pi}{2},$$

where $\bar{\phi}$ and $\bar{\theta}$ represent the mean values of azimuth and elevation angles, respectively, and κ is the shape factor and can be extracted from the measurement data.

As long as κ is determined, the time-variant angle of departure (AoD) and angle of arrival (AoA) can be obtained by $\bar{\phi}(t)$ and $\bar{\theta}(t)$, respectively, which can be expressed as follows:

$$\begin{aligned} \bar{\theta}_n^i(t) &= \arcsin\left(\frac{\mathbf{L}_z^{\text{S}^i}(t) - \mathbf{L}_z^i(t)}{\|\mathbf{L}^{\text{S}^i}(t) - \mathbf{L}^i(t)\|}\right), \\ \bar{\phi}_n^i(t) &= \begin{cases} \arccos\left(\frac{\mathbf{L}_x^{\text{S}^i}(t) - \mathbf{L}_x^i(t)}{\left(\|\mathbf{L}^{\text{S}^i}(t) - \mathbf{L}^i(t)\|\right) \cos(\bar{\theta}_n^i(t))}\right), & \mathbf{L}_y^{\text{S}^i}(t) - \mathbf{L}_y^i(t) \geq 0 \\ -\arccos\left(\frac{\mathbf{L}_x^{\text{S}^i}(t) - \mathbf{L}_x^i(t)}{\left(\|\mathbf{L}^{\text{S}^i}(t) - \mathbf{L}^i(t)\|\right) \cos(\bar{\theta}_n^i(t))}\right), & \mathbf{L}_y^{\text{S}^i}(t) - \mathbf{L}_y^i(t) < 0, \end{cases} \end{aligned} \quad (18)$$

where $i \in \{\text{MT}, \text{MR}\}$. Note that κ almost unchanged during the short simulation time period. Figure 2 gives an example of VMF distributed angles of AoA (or AoD) on the unit sphere with different parameters. It also reveals that with the

increase in shape factor κ , the shape of distribution becomes more concentrated.

4. Time-Variant Statistical Properties

The normalized spatial-temporal correlation function (STCF) between two different subchannels can be defined by [16, 19, 25]

$$\tilde{R}_{u_1, s_1, n}^{u_2, s_2, n}(t; \Delta t, \Delta \mathbf{d}) = \frac{E[\tilde{h}_{u_1, s_1, n}(t)\tilde{h}_{u_2, s_2, n}^*(t + \Delta t)]}{\sqrt{E[|\tilde{h}_{u_1, s_1, n}(t)|^2]E[|\tilde{h}_{u_2, s_2, n}(t + \Delta t)|^2]}} \quad (19)$$

where $E[\cdot]$ represents the expectation function, $(\cdot)^*$ is complex conjugate, and Δt means time lag. Moreover, $\Delta \mathbf{d} = \{\Delta \mathbf{d}^{\text{MT}}, \Delta \mathbf{d}^{\text{MR}}\}$ denotes the space lag and consists of $\Delta \mathbf{d}^{\text{MT}}$ and $\Delta \mathbf{d}^{\text{MR}}$, which are the corresponding space lags at two terminals, respectively. By substituting our proposed

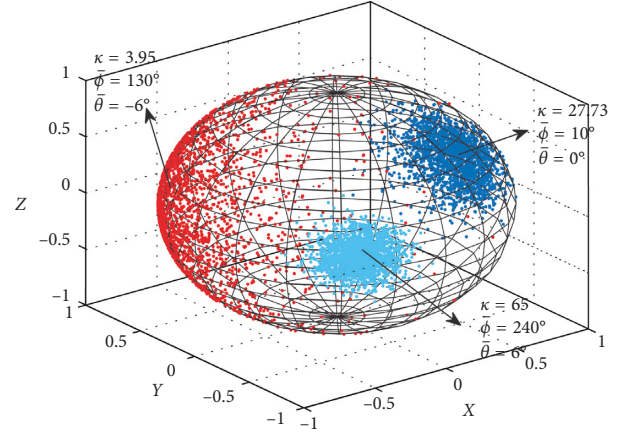


FIGURE 2: The VMF distributed angles on the unit sphere.

channel model (4) into (19), the expression of STCF can be obtained as

$$\begin{aligned} \tilde{R}_{u_1, s_1, n}^{u_2, s_2, n}(t; \Delta t, \Delta \mathbf{d}) &= \lim_{M \rightarrow \infty} \sqrt{\frac{1}{M}} \sum_{m=1}^M e^{j(\Phi_{u_2, s_2, n, m}^{\text{D}}(t+\Delta t) + \Phi_{u_2, s_2, n, m}^{\text{L}}(t+\Delta t) + \Phi_{n, m}^{\text{I}})} e^{-j(\Phi_{u_1, s_1, n, m}^{\text{D}}(t) + \Phi_{u_1, s_1, n, m}^{\text{L}}(t) + \Phi_{n, m}^{\text{I}})} \\ &= \iiint \int_{\{\theta_n^{\text{MT}}, \phi_n^{\text{MT}}, \theta_n^{\text{MR}}, \phi_n^{\text{MR}}\}} \sqrt{p(\phi_n^{\text{MT}}(t + \Delta t), \theta_n^{\text{MT}}(t + \Delta t))} \sqrt{p(\phi_n^{\text{MR}}(t + \Delta t), \theta_n^{\text{MR}}(t + \Delta t))} \\ &\quad \cdot \sqrt{p(\phi_n^{\text{MR}}(t), \theta_n^{\text{MR}}(t))} \cdot \sqrt{p(\phi_n^{\text{MT}}(t), \theta_n^{\text{MT}}(t))} e^{j(\Phi_{u_2, s_2, n}^{\text{D}}(t+\Delta t) - \Phi_{u_1, s_1, n}^{\text{D}}(t) + \Phi_{u_2, s_2, n}^{\text{L}}(t+\Delta t) - \Phi_{u_1, s_1, n}^{\text{L}}(t))} d\theta_n^{\text{MT}} d\phi_n^{\text{MT}} d\theta_n^{\text{MR}} d\phi_n^{\text{MR}}. \end{aligned} \quad (20)$$

4.1. Time-Variant SCFs. The SCFs is reduced from STCF when the time lag Δt equals to zero. Then, it can be expressed as

$$\tilde{R}_{u_1, s_1, n}^{u_2, s_2, n}(t; \Delta \mathbf{d}) = \iiint \int_{\{\theta_n^{\text{MT}}, \phi_n^{\text{MT}}, \theta_n^{\text{MR}}, \phi_n^{\text{MR}}\}} P(\phi_n^{\text{MT}}(t), \theta_n^{\text{MT}}(t)) P(\phi_n^{\text{MR}}(t), \theta_n^{\text{MR}}(t)) \cdot e^{j(\Phi_{u_2, s_2, n}^{\text{L}}(t) - \Phi_{u_1, s_1, n}^{\text{L}}(t))} d\theta_n^{\text{MT}} d\phi_n^{\text{MT}} d\theta_n^{\text{MR}} d\phi_n^{\text{MR}}. \quad (21)$$

Since the clusters S_n^{MT} and S_n^{MR} are independent, we can rewrite (21) as

$$\tilde{R}_{u_1, s_1, n}^{u_2, s_2, n}(t; \Delta \mathbf{d}) = \tilde{R}_n^{\text{MT}}(t; \Delta \mathbf{d}^{\text{MT}}) \cdot \tilde{R}_n^{\text{MR}}(t; \Delta \mathbf{d}^{\text{MR}}), \quad (22)$$

where $\tilde{R}_n^i(t; \Delta \mathbf{d}^i)$, $i \in \{\text{MT}, \text{MR}\}$, denotes the normalized SCF at the MT or MR. By substituting (7) into (21), the following equation can be obtained:

$$\begin{aligned} \tilde{R}_n^i(t; \Delta \mathbf{d}^i) &= \int_{-\pi}^{\pi} \int_{-\pi}^{\pi} e^{j\mathbf{k}(\tilde{s}_n^i(t))^{\text{T}} \cdot \mathbf{R}_v^i(t) \cdot \Delta \mathbf{d}^{i*}} \\ &\quad \cdot P_{\phi_{n, m}^i(t), \theta_{n, m}^i(t)}(\phi_n^i(t), \theta_n^i(t)) d\phi_n^i d\theta_n^i. \end{aligned} \quad (23)$$

It is shown in (23) that not only the angle of horizontal plane $\phi_n^i(t)$ but also the one of vertical plane $\theta_n^i(t)$ affects the

result of (23). Thus, traditional 2D models cannot obtain accurate correlation functions in 3D scattering environments. By setting $\theta_n^i(t) = \vec{\theta}_n^i(t) + \zeta$ and $\phi_n^i(t) = \vec{\phi}_n^i(t) + v$ and substituting them into (23), it yields

$$\tilde{R}_n^i(t; \Delta \mathbf{d}^i) = \int \int_{\{\zeta, v\}} \frac{\kappa \cos(\vec{\theta}_n^i(t) + \zeta) A^i B^i}{4\pi \sinh(\kappa)} d\zeta dv, \quad (24)$$

where

$$A^i = e^{\kappa (\cos(\vec{\theta}_n^i(t) + \zeta) \cos \vec{\theta}_n^i(t) \cos v + \sin(\vec{\theta}_n^i(t) + \zeta) \sin \vec{\theta}_n^i(t))}, \quad (25)$$

$$B^i = e^{j\mathbf{k}\tilde{s}(\vec{\phi}_n^i(t) + v, \vec{\theta}_n^i(t) + \zeta) \mathbf{R}_v^i(t) \Delta \mathbf{d}^{i*}}. \quad (26)$$

The measurement data demonstrate that the angle spread is usually narrow under V2V communication scenarios. With this assumption, we have $\cos(\zeta) \approx \cos(\nu) \approx 1$, $\sin(\zeta) \approx \zeta$, $\sin(\nu) \approx \nu$, $\kappa \cos(\nu) \approx \kappa(1 - \nu^2/2)$, and $\kappa \cos(\zeta) \approx \kappa(1 - \zeta^2/2)$. Consequently, we can rewrite (25) and (26) as

$$A^i \approx e^{\kappa(1-\zeta^2/2-2\cos^2(\bar{\theta}_n^i(t))(\nu/2)^2)}, \quad (27)$$

$$B^i \approx e^{jk(\bar{s}(\bar{\phi}_n^i(t), \bar{\theta}_n^i(t)) + C^i(t)\zeta + E^i(t)\nu)\mathbf{R}_V^i(t)\Delta \mathbf{d}^{i,t_0}}, \quad (28)$$

where

$$\mathbf{C}^i(t) = \left[-\sin \bar{\theta}_n^i(t) \cos \bar{\phi}_n^i(t), -\sin \bar{\theta}_n^i(t) \sin \bar{\phi}_n^i(t), \cos \bar{\theta}_n^i(t) \right], \quad (29)$$

$$\mathbf{D}^i(t) = \left[-\sin \bar{\phi}_n^i(t), \cos \bar{\phi}_n^i(t), 0 \right]. \quad (30)$$

By substituting (27)–(30) into (24) and using Euler formula, we can obtain the following equation:

$$\begin{aligned} \tilde{R}_n^i(t; \Delta \mathbf{d}^i) &\approx \frac{e^{jk\bar{s}(\bar{\phi}_n^i(t), \bar{\theta}_n^i(t))\mathbf{R}_V^i(t)\Delta \mathbf{d}^{i,t_0} + \kappa \cos(\bar{\theta}_n^i(t))}}{(\kappa^{1-m/2})(2\pi)^{m/2} I_{m/2-1}(\kappa)} \\ &\cdot \int_{-\Delta_\phi^i}^{\Delta_\phi^i} e^{-E^i(t)\nu^2} \cos(\mathbf{kD}^i(t)\mathbf{R}_V^i(t)\Delta \mathbf{d}^{i,t_0}\nu) d\nu \\ &\cdot \int_{-\Delta_\theta^i}^{\Delta_\theta^i} e^{-\kappa\zeta^2/2} \cos(\mathbf{kC}^i(t)\mathbf{R}_V^i(t)\Delta \mathbf{d}^{i,t_0}\zeta) d\zeta, \end{aligned} \quad (31)$$

where $E^i(t) = \kappa \cos^2(\bar{\theta}_n^i(t))/2$ and Δ_ϕ^i and Δ_θ^i are the angle spreads of AAoA and EAoA. With the help of integration formula,

$$\int_{-c}^c e^{-ax^2} \cos(bx) dx = \frac{j\sqrt{\pi}e^{-b^2/4a} (\operatorname{erfi}(b - 2jac)/2\sqrt{a}) - \operatorname{erfi}(b + 2jac/2\sqrt{a})}{2\sqrt{a}}. \quad (32)$$

The approximate closed-form result of SCF is as follows:

where $\operatorname{erfi}(\cdot)$ is the imaginary error function.

$$\begin{aligned} \tilde{R}_n^i(t; \Delta \mathbf{d}^i) &\approx \frac{-\operatorname{Im}(\operatorname{erfi}(F^i(t)))\operatorname{Im}(\operatorname{erfi}(G^i(t)))}{8 \sinh(\kappa)} \\ &\cdot e^{jk\bar{s}(\bar{\phi}_n^i(t), \bar{\theta}_n^i(t))\mathbf{R}_V^i(t)\Delta \mathbf{d}^{i,t_0}} \\ &\cdot e^{-(\mathbf{kR}_V^i(t)\Delta \mathbf{d}^{i,t_0})^2 \left((\mathbf{D}^i(t)/\sqrt{2\kappa})^2 + (\mathbf{C}^i(t)/\sqrt{2\kappa})^2 \right) + \kappa}, \end{aligned} \quad (33)$$

$$F^i(t) = \frac{\mathbf{kD}^i(t)\mathbf{R}_V^i(t)\Delta \mathbf{d}^{i,t_0} - j\kappa \cos^2(\bar{\theta}_n^i(t))\Delta_\phi^i}{\sqrt{2\kappa \cos^2(\bar{\theta}_n^i(t))}}, \quad (34)$$

$$G^i(t) = \frac{\mathbf{kC}^i(t)\mathbf{R}_V^i(t)\Delta \mathbf{d}^{i,t_0} - j\kappa \Delta_\theta^i}{\sqrt{2\kappa}}, \quad (35)$$

$$\begin{aligned} \tilde{R}_{u_1, s_1, n}^{u_1, s_1, n}(t; \Delta t) &= \int \int \int \int_{\{\theta_n^{\text{MT}}, \phi_n^{\text{MT}}, \theta_n^{\text{MR}}, \phi_n^{\text{MR}}\}} \sqrt{p(\phi_n^{\text{MT}}(t + \Delta t), \theta_n^{\text{MT}}(t + \Delta t))} \sqrt{p(\phi_n^{\text{MR}}(t + \Delta t), \theta_n^{\text{MR}}(t + \Delta t))} \sqrt{p(\phi_n^{\text{MR}}(t), \theta_n^{\text{MR}}(t))} \\ &\cdot \sqrt{p(\phi_n^{\text{MT}}(t), \theta_n^{\text{MT}}(t))} e^{j(\Phi_{u_1, s_1, n}^{\text{D}}(t) - \Phi_{u_1, s_1, n}^{\text{D}}(t + \Delta t) + \Phi_{u_1, s_1, n}^{\text{L}}(t) - \Phi_{u_1, s_1, n}^{\text{L}}(t + \Delta t))} d\theta_n^{\text{MT}} d\phi_n^{\text{MT}} d\theta_n^{\text{MR}} d\phi_n^{\text{MR}}, \end{aligned} \quad (36)$$

$$\tilde{R}_n^i(t; \Delta t) = \iint_{\{\phi_n^i, \theta_n^i\}} \sqrt{p(\phi_n^i(t), \theta_n^i(t))} \sqrt{p(\phi_n^i(t + \Delta t), \theta_n^i(t + \Delta t))} e^{-jk \int_t^{t+\Delta t} \mathbf{v}^{i, S_n}(t') \cdot \mathbf{s}_{n, m}^i(t') dt'} d\phi_n^i d\theta_n^i, \quad (37)$$

$$\begin{aligned} \tilde{R}_n^i(t; \Delta t) &= \frac{\kappa}{4\pi \sinh(\kappa)} \int_{-\Delta_\theta}^{\Delta_\theta} \int_{-\Delta_\phi}^{\Delta_\phi} \sqrt{\cos(\bar{\theta}_n^i(t) + \zeta) e^{\kappa(\cos(\bar{\theta}_n^i(t) + \zeta) \cos(\bar{\theta}_n^i(t)) \cos(v) + \sin(\bar{\theta}_n^i(t) + \zeta) \sin \bar{\theta}_n^i(t))}} \\ &\cdot \sqrt{\cos(\bar{\theta}_n^i(t + \Delta t) + \zeta) e^{\kappa(\cos(\bar{\theta}_n^i(t + \Delta t) + \zeta) \cos \bar{\theta}_n^i(t + \Delta t) \cos(v) + \sin(\bar{\theta}_n^i(t + \Delta t) + \zeta) \sin \bar{\theta}_n^i(t + \Delta t))}} \\ &\cdot e^{-jk \int_t^{t+\Delta t} \|\mathbf{v}^{i,S_n^i}(t)\| \left[\cos(\phi_v^{i,S_n^i}(t) - (\bar{\phi}_n^i(t) + v)) \cos(\bar{\theta}_n^i(t) + \zeta) \cos \theta_v^{i,S_n^i}(t) + \sin(\bar{\theta}_n^i(t) + \zeta) \sin \theta_v^{i,S_n^i}(t) \right] dt} dv d\zeta, \end{aligned} \quad (38)$$

$$\begin{aligned} \tilde{R}_n^i(t; \Delta t) &= \frac{\kappa}{4\pi \sinh(\kappa)} \int_{-\Delta_\theta}^{\Delta_\theta} \int_{-\Delta_\phi}^{\Delta_\phi} \sqrt{\cos(\bar{\theta}_n^i(t) + \zeta) e^{\kappa(\cos(\bar{\theta}_n^i(t) + \zeta) \cos(\bar{\theta}_n^i(t)) \cos(v) + \sin(\bar{\theta}_n^i(t) + \zeta) \sin \bar{\theta}_n^i(t))}} \\ &\cdot \sqrt{\cos(\bar{\theta}_n^i(t + \Delta t) + \zeta) e^{\kappa(\cos(\bar{\theta}_n^i(t + \Delta t) + \zeta) \cos \bar{\theta}_n^i(t + \Delta t) \cos(v) + \sin(\bar{\theta}_n^i(t + \Delta t) + \zeta) \sin \bar{\theta}_n^i(t + \Delta t))}} \\ &\cdot e^{-jk \|\mathbf{v}^{i,S_n^i}(t)\| \left[\cos(A^i(t; \Delta t; v, \zeta)) D^i(t; \Delta t) + \cos(B^i(t; \Delta t; v, \zeta)) E^i(t; \Delta t) + \sin(C^i(t; \Delta t; \zeta)) F^i(t; \Delta t) \right]} dv d\zeta. \end{aligned} \quad (39)$$

Finally, by substituting (33)–(35) into (22), the final result of SCF in our proposed model can be obtained. Due to time-variant communication environments, SCF is also time-dependent.

4.2. Time-Variant TCFs. The TCF is reduced from STCF when $\Delta \mathbf{d}$ is set to be zero. Then, TCF can be derived as (36). It also equals to the product of TCFs at the MT and MR $\tilde{R}_n^i(t; \Delta t)$, $i \in \{\text{MT}, \text{MR}\}$, when the clusters S_n^{MT} and S_n^{MR} are independent. For simplicity, we assumed that the antenna array is placed at the origin of the coordinate

system. By substituting (5) and (7) into (36), it can be obtained as (37).

By setting $\bar{\theta}_n^i(t) = \bar{\theta}_n^i(t) + \zeta$ and $\bar{\phi}_n^i(t) = \bar{\phi}_n^i(t) + v$ and substituting them into (37), it yields (38), where $\phi_v^{i,S_n^i}(t)$ and $\theta_v^{i,S_n^i}(t)$ mean the azimuth and elevation angles of the relative velocity between i and cluster S_n^i , respectively. It is reasonable to assume that the elevation AoDs and azimuth AoDs change linearly during the short time interval as $\bar{\phi}_n^i(t) = k_1 t + b_1$, $\bar{\theta}_n^i(t) = k_2 t + b_2$, where $k_1 = (\bar{\phi}_n^i(t + \Delta t_{\max}) - \bar{\phi}_n^i(t)) / \Delta t_{\max}$, $k_2 = (\bar{\theta}_n^i(t + \Delta t_{\max}) - \bar{\theta}_n^i(t)) / \Delta t_{\max}$, $b_1 = \bar{\phi}_n^i(t) - k_1 t$, and $b_2 = \bar{\theta}_n^i(t) - k_2 t$. By integrating the Doppler frequency, we can rewrite (38) as (39), where

$$\begin{aligned} A^i(t; \Delta t; v, \zeta) &= \left(\frac{t + \Delta t}{2} \right) (-k_1 + k_2) + \phi_v^{i,S_n^i}(t) - b_1 + b_2 - v + \zeta, \\ B^i(t; \Delta t; v, \zeta) &= \left(\frac{t + \Delta t}{2} \right) (-k_1 - k_2) + \phi_v^{i,S_n^i}(t) - b_1 - b_2 - v - \zeta, \\ C^i(t; \Delta t; \zeta) &= k_2 \left(\frac{t + \Delta t}{2} \right) + b_2 + \zeta, \\ D^i(t; \Delta t) &= \cos \theta_v^{i,S_n^i}(t) \sin \left(\frac{(\Delta t (-k_1 + k_2) / 2)}{(-k_1 + k_2)} \right), \\ E^i(t; \Delta t) &= \cos \theta_v^{i,S_n^i}(t) \sin \left(\frac{(\Delta t (k_1 + k_2) / 2)}{(k_1 + k_2)} \right), \\ F^i(t; \Delta t) &= 2 \sin \theta_v^{i,S_n^i}(t) \sin \left(\frac{(k_2 \Delta t / 2)}{k_2} \right), \\ \tilde{R}_n^i(t; \Delta t) &\approx \frac{\kappa e^\kappa}{4\pi \sinh(\kappa)} \sqrt{\cos(\bar{\theta}_n^i(t)) \cos(\bar{\theta}_n^i(t + \Delta t))} e^{-jk G^i(t; \Delta t)} \\ &\cdot \int_{-\Delta_\theta}^{\Delta_\theta} e^{-\kappa \zeta^2 / 2} \cos(k \Gamma^i(t; \Delta t) \zeta) d\zeta \cdot \int_{-\Delta_\phi}^{\Delta_\phi} e^{-j^i(t; \Delta t) v^2} \cos(k H^i(t; \Delta t) v) dv. \end{aligned} \quad (40)$$

$$\begin{aligned} \tilde{R}_n^i(t; \Delta t) &\approx \frac{\kappa e^\kappa}{4\pi \sinh(\kappa)} \sqrt{\cos(\bar{\theta}_n^i(t)) \cos(\bar{\theta}_n^i(t + \Delta t))} e^{-jk G^i(t; \Delta t)} \\ &\cdot \int_{-\Delta_\theta}^{\Delta_\theta} e^{-\kappa \zeta^2 / 2} \cos(k \Gamma^i(t; \Delta t) \zeta) d\zeta \cdot \int_{-\Delta_\phi}^{\Delta_\phi} e^{-j^i(t; \Delta t) v^2} \cos(k H^i(t; \Delta t) v) dv. \end{aligned} \quad (41)$$

Measurement data have revealed that small angle spreads exist under some scenarios. In other words, κ is usually big or ζ and v are small. Holding this condition, we have

$\cos(v - \zeta) \approx 1$, $\cos(v + \zeta) \approx 1$, $\sin(v - \zeta) \approx v - \zeta$, $\sin(v + \zeta) \approx v + \zeta$, $\cos(\zeta) \approx 1$, $\cos(v) \approx 1$, $\sin(\zeta) \approx \zeta$, and $\sin(v) \approx v$. Thus, we can approximate (39) as (41), where

$$\begin{aligned} G^i(t; \Delta t) &= \|\mathbf{v}^{i,S_n}(t)\| \cdot D^i(t; \Delta t) \cos(A^i(t; \Delta t)) + \|\mathbf{v}^{i,S_n}(t)\| \cdot E^i(t; \Delta t) \cos(B^i(t; \Delta t)) + \|\mathbf{v}^{i,S_n}(t)\| \cdot F^i(t; \Delta t) \sin(C^i(t; \Delta t)), \\ H^i(t; \Delta t) &= \|\mathbf{v}^{i,S_n}(t)\| \cdot D^i(t; \Delta t) \sin(A^i(t; \Delta t)) + \|\mathbf{v}^{i,S_n}(t)\| \cdot E^i(t; \Delta t) \sin(B^i(t; \Delta t)), \\ I^i(t; \Delta t) &= -\|\mathbf{v}^{i,S_n}(t)\| \cdot D^i(t; \Delta t) \sin(A^i(t; \Delta t)) + \|\mathbf{v}^{i,S_n}(t)\| \cdot E^i(t; \Delta t) \sin(B^i(t; \Delta t)) + \|\mathbf{v}^{i,S_n}(t)\| \cdot F^i(t; \Delta t) \cos(C^i(t; \Delta t)), \\ J^i(t; \Delta t) &= \frac{\kappa \left(\cos^2(\bar{\theta}_n^i(t)) + \cos^2(\bar{\theta}_n^i(t + \Delta t)) \right)}{4}, \end{aligned} \quad (42)$$

$$\begin{aligned} \bar{R}_n^i(t; \Delta t) &= \frac{\kappa}{8 \sinh(\kappa)} \sqrt{\cos(\bar{\theta}_n^i(t)) \cos(\bar{\theta}_n^i(t + \Delta t))} e^{\kappa - (k^2 I^i(t, \Delta t)/2\kappa) - (k^2 H^i(t, \Delta t)/4J^i(t, \Delta t)) - jkG^i(t, \Delta t)} \\ &\cdot \frac{\text{Im}(\text{erfi}(kH^i(t, \Delta t) - 2jJ^i(t, \Delta t)\Delta_\phi/2\sqrt{J^i(t, \Delta t)}))}{\sqrt{J^i(t, \Delta t)}} \frac{\text{Im}(\text{erfi}((kI^i(t, \Delta t) - jk\Delta_\theta/\sqrt{2\kappa})))}{\sqrt{2\kappa}} \end{aligned} \quad (43)$$

where $A^i(t; \Delta t)$, $B^i(t; \Delta t)$, and $C^i(t; \Delta t)$ are the value of $A^i(t; \Delta t; v, \zeta)$, $B^i(t; \Delta t; v, \zeta)$, and $C^i(t; \Delta t; \zeta)$ when $v = \zeta = 0$, respectively. Using the integration formula in (32), the closed-form expression of (41) can be expressed as (43). On this basis, we can obtain the final TCF expression of the proposed model.

4.3. Time-Variant DPSDs. The DPSD is the Fourier transform of TCF $\bar{R}_{u,s,n}(t; \Delta t)$. For the nonstationary aspect of our proposed model, the DPSD can be calculated with short-time Fourier transform as

$$S_n(f; t) = \int_{-\infty}^{\infty} \bar{R}_{u,s,n}(t; \Delta t) e^{-j2\pi f \Delta t} \nu(t - \Delta t) d\Delta t, \quad (44)$$

where window function $\nu(t - \Delta t)$ lasting time is shorter than the stationary interval (about several milliseconds [10]).

5. Simulation Results and Validation

Firstly, in order to evaluate the accuracy of our derived SCF and TCF, we calculate the maximum difference between the approximated and numerical integral results over $\bar{\phi}_n^i \in [-180^\circ, 180^\circ]$ and $\bar{\theta}_n^i \in [-10^\circ, 10^\circ]$. Figure 3 shows the results of maximum absolute error with different κ , normalized space lags, and time lags. As we can see that the maximum absolute error of SCF is less than 0.025 when κ is more than 50 and d/λ is less than 3, and it increases as κ decreases or d/λ increases. Meanwhile, the absolute error of TCF is less than 0.02 when κ is more than 50 and the time lag is less than 0.05 s, and it increases as κ decreases or the time lag increases. Overall, the maximum error is acceptable, and thus, the derived expressions can be used to calculate the SCF and TCF efficiently.

Secondly, in order to verify the generality of the proposed channel model. Three V2V communication scenarios with different trajectories are selected and given in Figure 4. In the figure, the MT travels straightly with the fixed velocity, and the MR travels in three different velocities with the same departure and arrival points. Path I has fixed speed and travel direction, and Path II allows speed variation with 2D direction movement. Furthermore, Path III has 3D variations in both vertical and horizontal directions. For demonstration purpose, the distribution of clusters is uniform, and we adopt VMF distribution to depict AoAs and AoDs and set κ as 3.95 [39]. With the referred data in [41], we assume that the speeds of cluster are Gaussian-distributed with 1 km/h mean value and 0.1 variance. Furthermore, the carrier frequency $f_c = 2.4$ GHz, $\phi_{v_n}^{\text{SMI}}$, $\phi_{v_n}^{\text{SMR}}$, $\theta_{v_n}^{\text{SMI}}$ and $\theta_{v_n}^{\text{SMR}}$ are all uniformly distributed. The former pair distributes over 0 and 2π , but the later one only distributes over $-\pi/36$ and $\pi/36$.

It should be mentioned that the V2V channel models in [11–26, 28, 30] only considered fixed velocities of two terminals like Path I, while the models in [31–33] allowed for 2D curve trajectories like Path II. The absolute values of the theoretical SCFs of different models including the model considering Path I in [30] and the one focusing on Path II in [32] are simulated and compared in Figure 5. The good agreement of SCFs between our proposed and other models indicates the generalization and compatibility of our proposed model. In particular, the models in [30, 32] can be viewed as two special applications in straight or curved trajectories.

Thirdly, in order to verify the correctness of statistical properties of our proposed model under 3D trajectories like Path III, the theoretical, approximated, and simulated values of SCFs and TCFs are shown in Figure 6. The x -axis of Figure 6(a) represents normalized space between antennas,

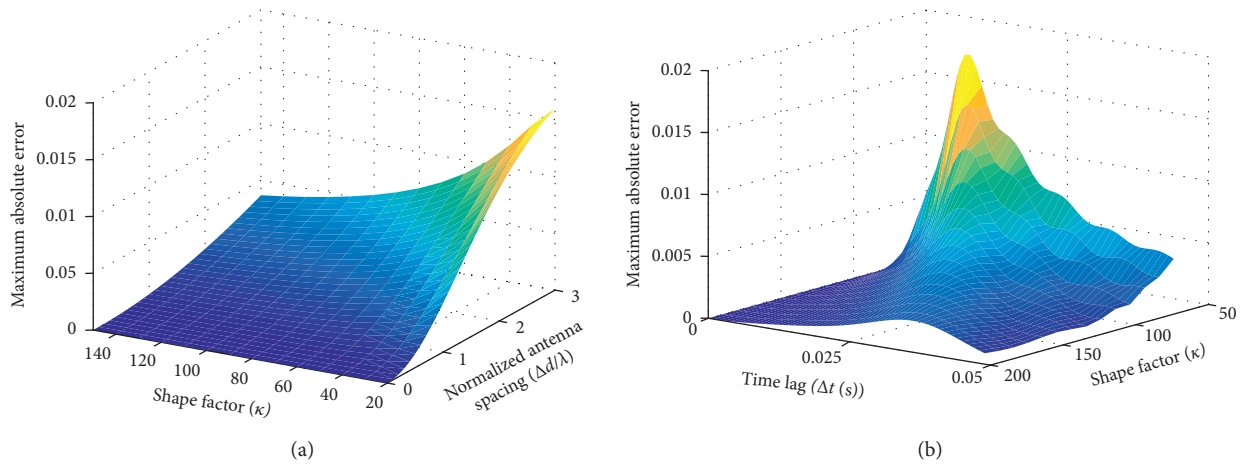


FIGURE 3: Maximum absolute errors between the theoretical and approximate (a) SCFs and (b) TCFs.

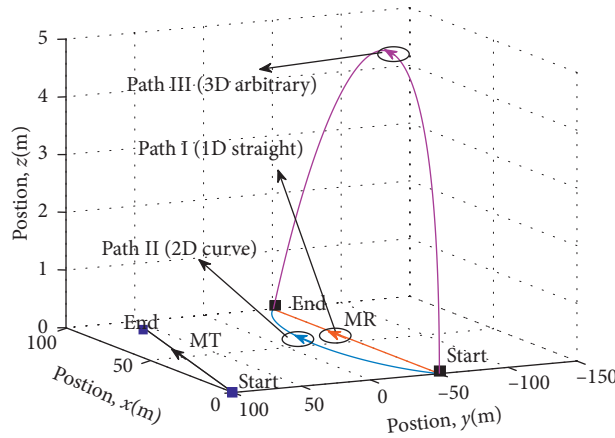


FIGURE 4: Three typical trajectories of the MR.

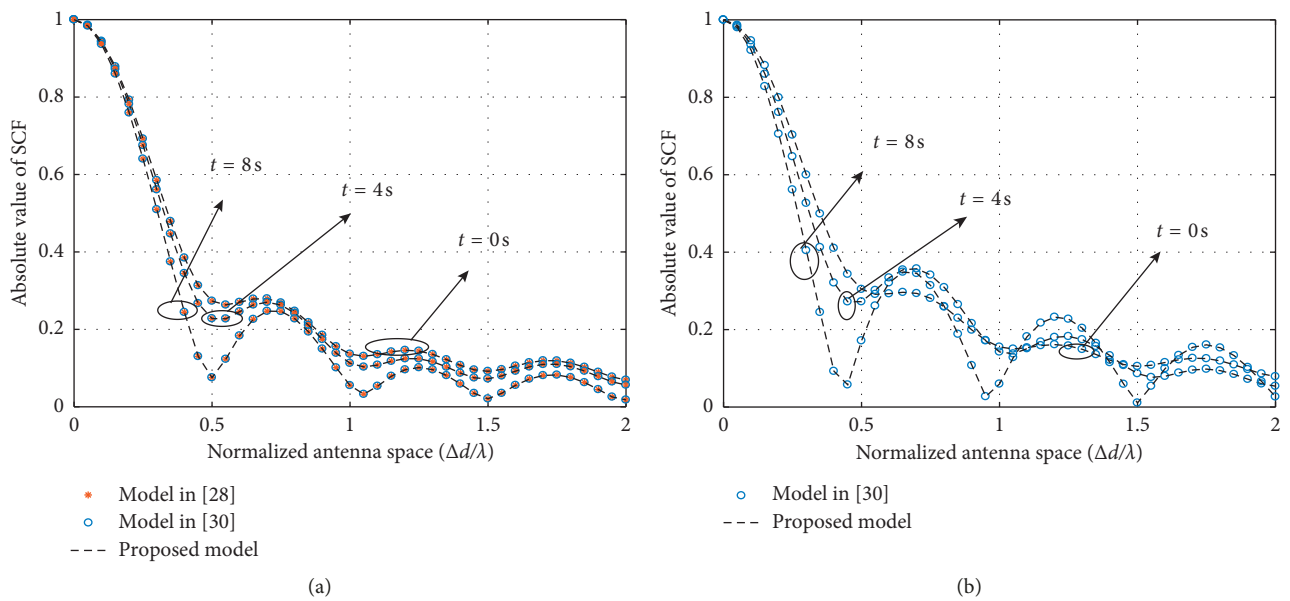


FIGURE 5: Comparison of absolute SCFs for (a) Path I and (b) Path II.

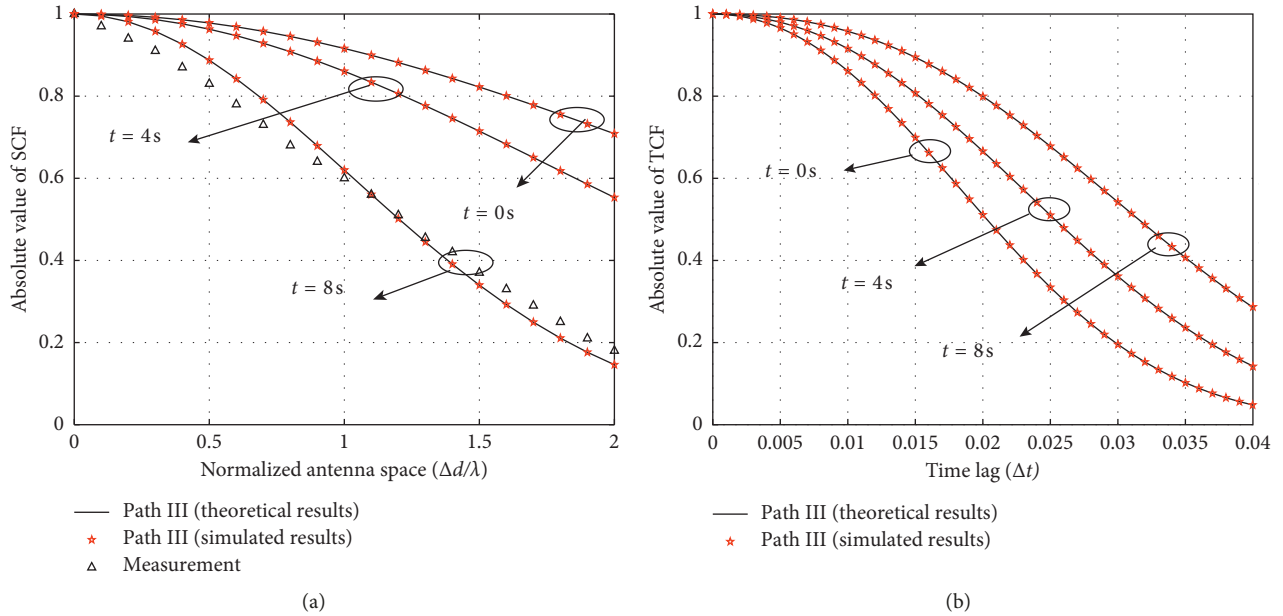


FIGURE 6: Comparison of absolute theoretical and simulated (a) SCFs and (b) TCFs at different time instants.

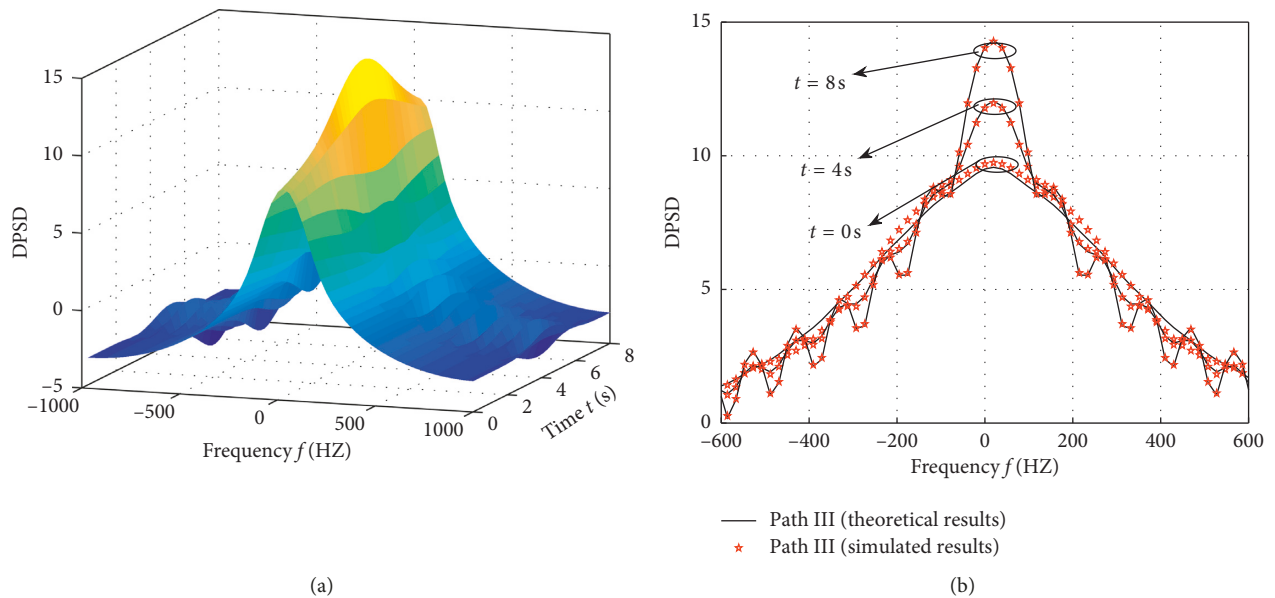


FIGURE 7: (a) Theoretical 3D DPSD and (b) theoretical and simulated DPSDs at different time instants for Path III.

which is similar at two terminals in the communication system. By substituting $u_1 = s_1 = 1$, $u_2 = s_2 = 2$, and $n = 1$ into (21) and (33), we can get the theoretical and approximated values of SCFs. In addition, the measured results in [42] are also shown in Figure 6(a). The good agreement of SCFs shows the correctness of both the theoretical model and derivations. Similarly, by substituting $u = s = 1$ and $n = 1$ into (36) and (43), we obtain and show the theoretical and approximated values of TCFs in Figure 6(b). The good agreements between theoretical, simulated, and approximated results reveal that our simulation and derivation are correct.

Finally, substituting TCFs into (44), we can get the theoretical and simulated values of DPSDs for Path III, which are also shown in Figure 7. It clearly shows that moving clusters and two terminals have an influence on the drifting of DPSDs. Moreover, good agreements between the simulated and theoretical results indicate that our proposed model is correct.

6. Conclusion

This paper has proposed a general channel model characterized by 3D scattering environments, 3D movements, and

3D-shaped antenna arrays of two terminals for V2V communication system. The upgraded algorithms for time-evolving parameters such as the number of paths, path delays, path powers, and angles have been developed and analyzed in detail. Meanwhile, the approximated expressions of statistical properties including SCF, TCF, and DPSD have been derived and verified by simulations. Simulated and analyzed results show that different moving trajectories significantly affect the V2V channel characteristic. Meanwhile, the generalization and compatibility of our proposed model also demonstrate that some previous models with 2D or even 1D movements have special applications. The new model can be used to develop, analyze, and test realistic V2V communication systems in the future.

Data Availability

The data used to support the findings of this study are available from the corresponding author upon request.

Conflicts of Interest

The authors declare that they have no conflicts of interest.

Acknowledgments

This work was supported by the National Key Scientific Instrument and Equipment Development Project (Grant no. 61827801), Aeronautical Science Foundation of China (Grant no. 2017ZC52021), and Open Foundation for Graduate Innovation of NUAU (Grant no. KFJJ 20180408).

References

- [1] C.-X. Wang, X. Cheng, and D. I. Laurenson, "Vehicle-to-vehicle channel modeling and measurements: recent advances and future challenges," *IEEE Communications Magazine*, vol. 47, no. 11, pp. 96–103, 2009.
- [2] K. Guan, B. Ai, M. Liso Nicolas et al., "On the influence of scattering from traffic signs in vehicle-to-x communications," *IEEE Transactions on Vehicular Technology*, vol. 65, no. 8, pp. 5835–5849, 2016.
- [3] X. Cheng, C.-X. Wang, B. Ai, and H. Aggoune, "Envelope level crossing rate and average fade duration of nonisotropic vehicle-to-vehicle rician fading channels," *IEEE Transactions on Intelligent Transportation Systems*, vol. 15, no. 1, pp. 62–72, 2014.
- [4] Q. Zhu, C. Xue, X. Chen, and Y. Yang, "A new MIMO channel model incorporating antenna effects," *Progress In Electromagnetics Research M*, vol. 50, pp. 129–140, 2016.
- [5] A. G. Zajic and G. L. Stubber, "Space-time correlated mobile-to-mobile channels: modelling and simulation," *IEEE Transactions on Vehicular Technology*, vol. 57, no. 2, pp. 715–726, 2008.
- [6] W. Fan, X. Carreno Bautista de Lisboa, F. Sun, J. O. Nielsen, M. B. Knudsen, and G. F. Pedersen, "Emulating spatial characteristics of MIMO channels for OTA testing," *IEEE Transactions on Antennas and Propagation*, vol. 61, no. 8, pp. 4306–4314, 2013.
- [7] J. Zhang, Y. Zhang, Y. Yu, R. Xu, Q. Zheng, and P. Zhang, "3-D MIMO: how much does it meet our expectations observed from channel measurements?," *IEEE Journal on Selected Areas in Communications*, vol. 35, no. 8, pp. 1887–1903, 2017.
- [8] J. Karedal, F. Tufvesson, N. Czink et al., "A geometry-based stochastic MIMO model for vehicle-to-vehicle communications," *IEEE Transactions on Wireless Communications*, vol. 8, no. 7, pp. 3646–3657, 2009.
- [9] A. Paier, T. Zemen, L. Bernado et al., "Non-WSSUS vehicular channel characterization in high-way and urban scenarios at 5.2 GHz using the local scattering function," in *Proceedings of the 2008 International ITG Workshop on Smart Antennas*, pp. 9–15, Darmstadt, Germany, February 2008.
- [10] R. He, O. Renaudin, V.-M. Kolmonen et al., "Characterization of quasi-stationarity regions for vehicle-to-vehicle radio channels," *IEEE Transactions on Antennas and Propagation*, vol. 63, no. 5, pp. 2237–2251, 2015.
- [11] Y. Ma, L. Yang, and X. Zheng, "A geometry-based non-stationary MIMO channel model for vehicular communications," *China Communications*, vol. 15, no. 7, pp. 30–38, 2018.
- [12] C. A. Gutierrez, J. T. Gutierrez-Mena, J. M. Luna-Rivera, D. U. Campos-Delgado, R. Velquez, and M. Patzold, "Geometry-based statistical modeling of non-WSSUS mobile-to-mobile Rayleigh fading channels," *IEEE Transactions on Vehicular Technology*, vol. 67, no. 1, pp. 362–377, 2018.
- [13] A. Chelli and M. Patzold, "A non-stationary MIMO vehicle-to-vehicle channel model derived from the geometrical street model," in *Proceedings of the Vehicular Technology Conference*, pp. 1–6, San Francisco, CA, USA, September 2011.
- [14] A. Borhani and M. Patzold, "Correlation and spectral properties of vehicle-to-vehicle channels in the presence of moving scatterers," *IEEE Transactions on Vehicular Technology*, vol. 62, no. 9, pp. 4228–4239, 2013.
- [15] H. Jiang, Z. Zhang, L. Wu, and J. Dang, "Novel 3-D irregular-shaped geometry-based channel modeling for semi-ellipsoid vehicle-to-vehicle scattering environments," *IEEE Wireless Communications Letters*, vol. 7, no. 5, pp. 836–839, 2018.
- [16] A. G. Zajic, "Impact of moving scatterers on vehicle-to-vehicle narrow-band channel characteristics," *IEEE Transactions on Vehicular Technology*, vol. 63, no. 7, pp. 3094–3106, 2014.
- [17] X. Zhao, X. Liang, S. Li, and B. Ai, "Two-cylinder and multi-ring GBSSM for realizing and modeling of vehicle-to-vehicle wideband MIMO channels," *IEEE Transactions on Intelligent Transportation Systems*, vol. 17, no. 10, pp. 2787–2799, 2016.
- [18] Y. Bi, J. Zhang, M. Zeng, M. Liu, and X. Xu, "A novel 3D nonstationary channel model based on the von Mises-Fisher scattering distribution," *Mobile Information Systems*, vol. 2016, Article ID 2161460, pp. 1–9, 2016.
- [19] Y. Yuan, C.-X. Wang, Y. He, M. M. Alwakeel, and E.-H. M. Aggoune, "3D wideband non-stationary geometry-based stochastic models for non-isotropic MIMO vehicle-to-vehicle channels," *IEEE Transactions on Wireless Communications*, vol. 14, no. 12, pp. 6883–6895, 2015.
- [20] N. Avazov, S. M. R. Islam, D. Park, and K. S. Kwak, "Statistical characterization of a 3-D propagation model for V2V channels in rectangular tunnels," *IEEE Antennas and Wireless Propagation Letters*, vol. 16, pp. 2392–2395, 2017.
- [21] H. Jiang, Z. Zhang, J. Dang, and L. Wu, "A novel 3-D massive MIMO channel model for vehicle-to-vehicle communication environments," *IEEE Transactions on Communications*, vol. 66, no. 1, pp. 79–90, 2018.
- [22] N. Avazov, S. M. R. Islam, D. Park, and K. S. Kwak, "Cluster-based non-stationary channel modeling for vehicle-to-vehicle communications," *IEEE Antennas and Wireless Propagation Letters*, vol. 16, pp. 1419–1422, 2016.

- [23] D. Du, X. Zeng, X. Jian, L. Miao, and H. Wang, "Three-dimensional vehicle-to-vehicle channel modeling with multiple moving scatterers," *Mobile Information Systems*, vol. 2017, Article ID 7231417, pp. 1–14, 2017.
- [24] X. Liang, W. Cao, and X. Zhao, "Doppler power spectra for 3D vehicle-to-vehicle channels with moving scatterers," *IEEE Access*, vol. 6, pp. 42822–42828, 2018.
- [25] X. Chen, Y. Fang, Y. Sun, Y. Pan, and W. Xiang, "Statistical characterization of novel 3D cluster-based MIMO vehicle-to-vehicle models for urban street scattering environments," *International Journal of Antennas and Propagation*, vol. 2018, Article ID 6742346, pp. 1–11, 2018.
- [26] Q. Zhu, H. Li, Y. Fu et al., "A novel 3D non-stationary wireless MIMO channel simulator and hardware emulator," *IEEE Transactions on Communications*, vol. 66, no. 9, pp. 3865–3878, 2018.
- [27] K. Jiang, X. Chen, Q. Zhu, L. Chen, D. Xu, and B. Chen, "A novel simulation model for nonstationary rice fading channels," *Wireless Communications and Mobile Computing*, vol. 2018, Article ID 8086073, pp. 1–9, 2018.
- [28] M. Patzold, C. A. Gutierrez, and N. Youssef, "On the consistency of non-stationary multipath fading channels with respect to the average doppler shift and the doppler spread," in *Proceedings of the IEEE Wireless Communications and Networking Conference (WCNC)*, pp. 1–6, San Francisco, CA, USA, 2017.
- [29] Q. Zhu, W. Li, C.-X. Wang et al., "Temporal correlations for a non-stationary vehicle-to-vehicle channel model allowing velocity variations," *IEEE Communications Letters*, vol. 23, no. 7, pp. 1280–1284, 2019.
- [30] Q. Zhu, Y. Yang, X. Chen et al., "A novel 3D non-stationary vehicle-to-vehicle channel model and its spatial-temporal correlation properties," *IEEE Access*, vol. 6, pp. 43633–43643, 2018.
- [31] W. Dahech, M. Patzold, and N. Youssef, "A non-stationary mobile-to-mobile multipath fading channel model taking account of velocity variations of the mobile stations," in *Proceedings of the IEEE International Symposium on Antennas and Propagation*, pp. 1–4, Lisbon, Portugal, April 2015.
- [32] W. Dahech, M. Patzold, C. A. Gutierrez, and N. Youssef, "A non-stationary mobile-to-mobile channel model allowing for velocity and trajectory variations of the mobile stations," *IEEE Transactions on Wireless Communications*, vol. 16, no. 3, pp. 1987–2000, 2017.
- [33] C. A. Gutierrez, M. Patzold, W. Dahech, and N. Youssef, "A non-WSSUS mobile-to-mobile channel model assuming velocity variations of the mobile stations," in *Proceedings of the Wireless Communications and Networking Conference (WCNC)*, pp. 1–6, San Francisco, CA, USA, March 2017.
- [34] Q. Zhu, Y. Yang, C. X. Wang et al., "Spatial correlations of a 3D non-stationary MIMO channel model with 3D antenna arrays and 3D arbitrary trajectories," *IEEE Wireless Communications Letters*, vol. 8, no. 2, pp. 512–515, 2019.
- [35] Y. Yang, Q. Zhu, W. Li et al., "A general 3D non-stationary twin-cluster model for vehicle-to-vehicle MIMO channels," in *Proceedings of the Wireless Communications and Signal Processing*, pp. 1–6, Hangzhou, China, October 2018.
- [36] H. Hofstetter, A. F. Molisch, and N. Czink, "A twin-cluster MIMO channel model," in *Proceedings of the Antennas and Propagation (EuCAP)*, pp. 1–8, Nice, France, November 2006.
- [37] I. Sen and D. W. Matolak, "Vehicle-vehicle channel models for the 5-GHz band," *IEEE Transactions on Intelligent Transportation Systems*, vol. 9, no. 2, pp. 235–245, 2008.
- [38] T. Zwick, C. Fischer, D. Didascalou, and W. Wiesbeck, "A stochastic spatial channel model based on wave-propagation modeling," *IEEE Journal on Selected Areas in Communications*, vol. 18, no. 1, pp. 6–15, 2000.
- [39] K. Mammassis and R. W. Stewart, "The Fisher-Bingham spatial correlation model for multielement antenna systems," *IEEE Transactions on Vehicular Technology*, vol. 58, no. 5, pp. 2130–2136, 2009.
- [40] M. Konstantinos, S. W. Robert, and J. S. Thompson, "Spatial fading correlation model using mixtures of Von Mises Fisher distributions," *IEEE Transactions on Wireless Communications*, vol. 8, no. 4, pp. 2046–2055, 2009.
- [41] A. Fayziyev, M. Patzold, E. Masson, Y. Cocheril, and M. Berbineau, "A measurement-based channel model for vehicular communications in tunnels," in *Proceedings of the Wireless Communications and Networking Conference (WCNC)*, pp. 116–121, Istanbul, Turkey, April 2014.
- [42] S. Payami and F. Tufvesson, "Channel measurements and analysis for very large array systems at 2.6 GHz," in *Proceedings of the Antennas and Propagation (EuCAP)*, pp. 433–437, Prague, Czech Republic, March 2012.



Hindawi

Submit your manuscripts at
www.hindawi.com

